Fermilab

FERMILAB-Pub-02/187 August 2002

# Beam test results of the US-CMS forward pixel detector ☆

M. Atac[a], E. Bartz[b], G. Bolla[c], D. Bortoletto[c], C.Y. Chien[d], L. Cremaldi[e], J. Doroshenko[b], K. Giolo[c], B. Gobbi[f], P. Gomez[g], G. Grim[g], T. Koeth[b], Y. Kozhevnikov[a], R. Lander[g], S. Malik[f], D. Pellett[g], L. Perera[b], M. Pernicka[h], C. Rott[c,*], A. Roy[c], D. Sanders[e], S. Schnetzer[b], H. Steininger[h], R. Stone[b], M. Swartz[d], R. Tilden[f], X. Xie[d]

[a] *Fermi National Accelerator Laboratory, MS 318-P.O. Box 500, Batavia, IL 60510, USA*
[b] *Rutgers University, Piscataway, NJ 08854, USA*
[c] *Purdue University, West Lafayette, IN 47907, USA*
[d] *Johns Hopkins University, Baltimore, MD 21218, USA*
[e] *University of Mississippi, Oxford, MS 38677, USA*
[f] *Northwestern University, Evanston, IL 60201, USA*
[g] *University of California, Davis, CA 95616, USA*
[h] *Institut für Hochenergiephysik, Österr. Akad. d. Wissensch., Vienna A-1050, Austria*

**Abstract**

CMS will use silicon pixel as its innermost tracking device. Prototypes of these 150 μm square pixels bump bonded to DMILL readout chips were tested at CERN in a pion beam. A silicon telescope consisting of 8 planes of silicon strips was used to interpolate tracks to the position of the pixel detector. Data were taken with the beam at different angles of incidence relative to the pixel sensors. Position resolutions between 10 and 20 μm, depending on the hit position, were observed using charge sharing for the final configuration with unirradiated detectors. The observed resolution was as expected. © 2002 Elsevier Science B.V. All rights reserved.

*PACS:* 29.40.Wk

*Keywords:* CMS; Forward; Pixel; FPIX; Beam test; Resolution

## 1. Introduction

The pixel detector will be the innermost part of the CMS tracker. It will use 150 μm square silicon pixels with a thickness of about 270 μm. The tracking performance will profit from the 4 T magnetic field of CMS along the beam axis creating $E \times B$ charge sharing effects in the pixel barrel. For the disks the sensors will be rotated by

This work has been supported partly by the DOE grant DE-FG02-91ER40681 (Task G) and NSF Early Career Award. We would also like to thank Roland Horisberger for designing and providing the readout chip. We thank for the support we received from CERN, PSI, Aachen, and Vienna.

*Corresponding author. Fermi National Accelerator Laboratory, MS 318-P.O. Box 500, Batavia, IL 60510, USA. Tel.: +1-630-840-2308.

*E-mail address:* carott@physics.purdue.edu (C. Rott).

20° around their central radial axis, to introduce a component of the electric field that is perpendicular to the magnetic field. Thereby $E \times B$ charge sharing effects will be created in the disks as well as geometric charge sharing is increased in $r$–$\phi$. Hence, we expect initially resolutions of 15 μm in the forward disks as given in the TDR [1]. These charge sharing effects were studied with prototype detectors at the SPS at CERN in the summer of 2000. We used the beam lines X5, X7 and H2 with $\pi^+$ of momentum up to 250 GeV/$c$.

## 2. The pixel sensors

The pixel detectors used during the beam test were 150 μm square pixels fabricated by Sintef from 270 μm thick silicon of ⟨1 0 0⟩ orientation. The pixels were arranged in an array of 22 columns and 30 rows. Four-inch wafers containing several different pixel arrays with different p-stop designs were tested [2]. Previously the depletion voltage was found to be between 140 and 170 V. Pixel sensors fulfilling the requirements for the CMS pixel system were then bump bonded to custom made, radiation hard DMILL readout chips (PSI36) with a readout architecture similar to the ones described in Ref. [3]. The bump bonded detectors were then shipped to CERN. Pixels having the step double ring p-stop design, shown in Fig. 1, were used in the beam test. The pixel sensors were operated at room temperature and a reverse bias voltage of 220 V was applied, in order to ensure at least 50 V over depletion.

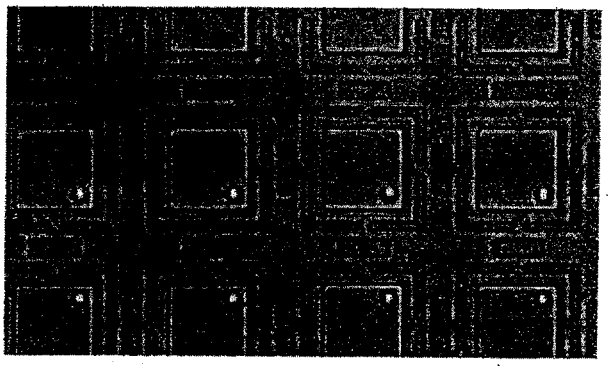

Fig. 1. Sintef 150 μm silicon square pixels having the step double ring p-stop design.

## 3. The telescope

A telescope consisting of 8 single sided silicon strip detectors was used to interpolate tracks into the DUT (Device Under Test). The readout was triggered on a coincidence using a large upstream and downstream scintillator and a scintillating fiber array. The fibers, which could be chosen individually for triggering, had a diameter of 1 mm and therefore allowed triggering on a small area. This proved to be very useful, since the dimensions of the DUT were very small. Fig. 2 shows a schematic plot of the telescope.

The pixel sensor bump bonded to the ROC (Readout Chip) was connected to an extension card, which was connected to the Vienna PSI30 repeater card. The repeater card was used to control the voltage settings of the ROC and was located at the center of the telescope. The silicon strip planes of the telescope were arranged in an alternating order of horizontal and vertical strip planes. The silicon strips consisted of 2 × 128 parallel strips with a strip pitch of 50 μm and showed residual resolutions of about 5 μm. For the alignment of the strip planes the first pair of horizontal and vertical silicon strip planes served as a reference system and it was assumed that they were perpendicular with respect to each other. The following strip planes were aligned with respect to them by correcting for rotations around the beam axis. The best alignment was achieved by minimizing the variation in the hit position of beam particles between the reference strip plane and the strip plane under alignment.

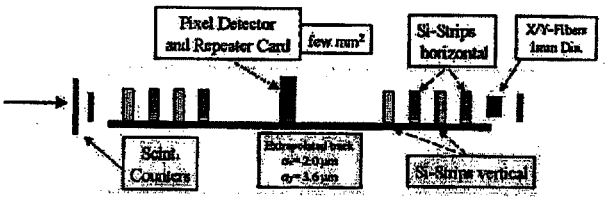


Fig. 2. The telescope as used during the beam test.

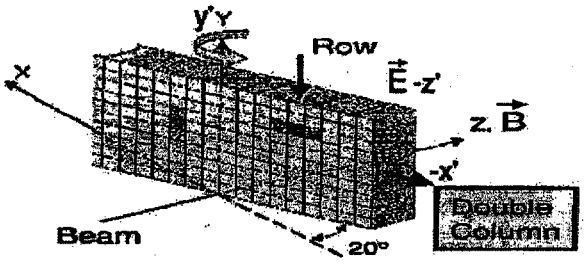


Fig. 3. The sensor and telescope coordinate system.

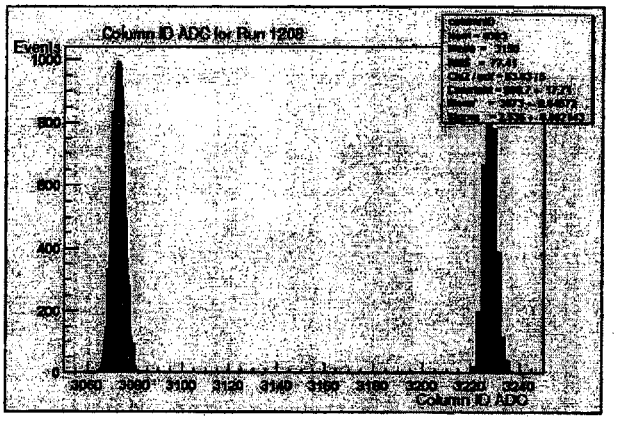


Fig. 4. Distributions of two neighboring double columns is shown. It can clearly be distinguished between different double columns.

After alignment interpolated tracks to the center of the telescope yielded a resolution of 2.0 μm in horizontal and 3.6 μm in vertical direction.

For this analysis two coordinate systems were used as seen in Fig. 3. The telescope system $(x,y,z)$, where $z$ was defined as pointing in direction of the beam and $x$ and $y$ as the horizontal and vertical direction, defined by the silicon strips. The second coordinate system used was the sensor system $(x',y',z')$. Where $x'$ was along the pixel double columns (horizontal), $y'$ along the pixel rows (vertical). $z'$ was perpendicular to $x'$ and $y'$ running from the back plane (which was facing the beam) to the pixel side of the sensor. To investigate charge sharing effects, the sensor could be rotated around the $y$-axis, where the angle between $x$ and $x'$ was defined as $\alpha$, the rotation angle of the sensor. In an ideal case for $\alpha = 0°$ the sensor and telescope system should have been identical. Corrections were applied to take into account possible misalignments between the two reference systems.

## 4. Beam test results

The prototype sensor used during the beam test consisted of a 30 × 22 pixel array. The pixels were grouped into 30 rows and 11 double columns. If one pixel in a double column was above a programmable threshold, the whole double column was read out. The analog output was then digitized by a 40 MHz 12-bit ADC.

### *4.1. Double column ID*

To distinguish between the 11 double columns of the DUT, a voltage level, from now called DCID (Double Column Identifier), was embedded into the analog output. The difference between the DCIDs of two neighboring double columns was about 160 ADC, while the distribution of a single DCID had a $\sigma \simeq 2.5$ADC. Hence, we could clearly separate between different double columns, as seen in Fig. 4.

### *4.2. Calibration*

A calibration of the front-end electronics was performed to find the number of electrons corresponding to one ADC count. Each pixel cell is equipped with a calibration capacitor (nominal value 1.7 fF) that could be connected to the input of the preamplifier via a programmable switch. The schematic of the FE analog block is shown in Fig. 5. The repeater card generated a step function that was injected into such capacitor. Plotting the output of a pulsed channel versus the amplitude of the step function we measured a slope of $1\text{ADC} \simeq 17.1\text{e}^-$, as seen in Fig. 6.

### *4.3. Pulse height and noise*

The chip used was the PSI36 developed at PSI (Paul Scherrer Institut) and fabricated in DMILL

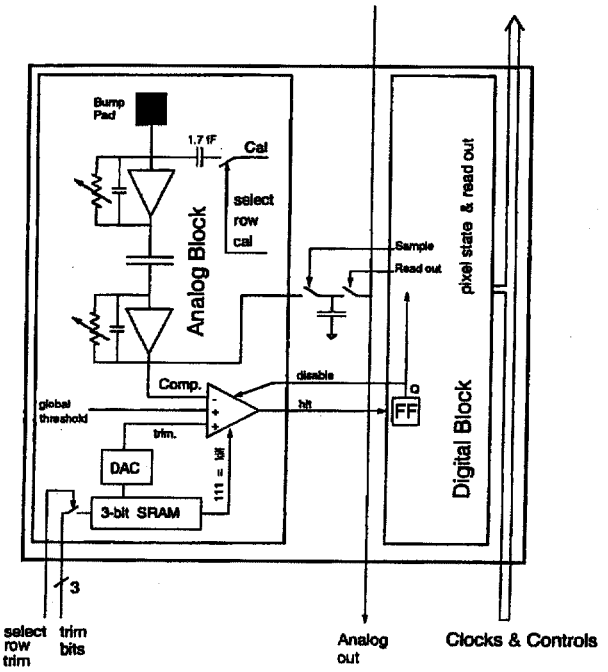


Fig. 5. Schematics block diagram of the pixel unit cell on the readout chip. The calibration capacitor can be seen on the top part of the analog block.

process. During data taking the noise level was anomalously high. With diamond pixel sensors [4] that were read out with a slightly different version of the ROC fabricated in HONEYWELL process and exactly the same DAQ the noise level was as expected. Such extra noise is yet to be understood and is probably due to our short experience with the electronics combined with a noisy prototype of the ROC. Noise increased as more double columns were enabled. Therefore data were taken enabling only a single double column. To optimize the noise performance of the analog electronics the bias voltages for the preamplifier stage, its feedback transistor and the source follower had to be fine-tuned. At this prototype phase, no limits were imposed on the chip power consumption. The used set of voltages is listed in Table 1 and was chosen in order to minimize the noise. A more detailed description of these settings is given in Ref. [5].

A further reduction in noise was achieved by proper grounding. It was observed that the remaining noise consisted mainly of common mode noise. This coherent noise was calculated

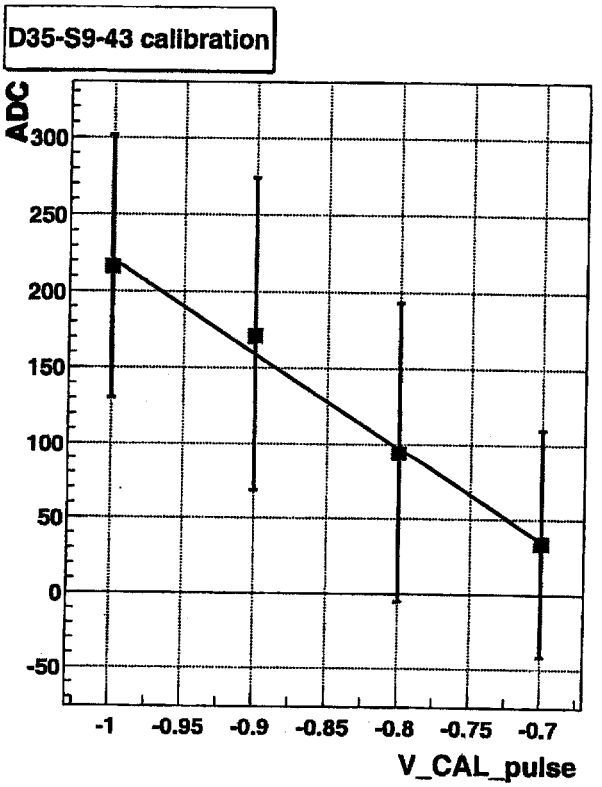


Fig. 6. Calibration with the internal pulser gave 1ADC≃ 17.1e⁻. The vertical axis shows ADC corresponding to the voltage of the calibration pulse.

Table 1
Voltage setting for the Vienna PSI30 repeater card as used during the beam test

| | Voltage (V) | Description |
|---|---|---|
| $V_C$ | − 2.60 | Threshold voltage |
| $V_A$ | − 2.53 | Supply voltage for the preamplifier and shaper |
| $V_{SF}$ | − 3.31 | Supply voltage of source followers behind preamplifier and shaper |

by plotting the event pedestal of a single pixel versus the average pedestal across the double column for the same event. As it can be seen from Fig. 7 the correlation is very strong.

In the following analysis corrections were applied to subtract the coherent noise.

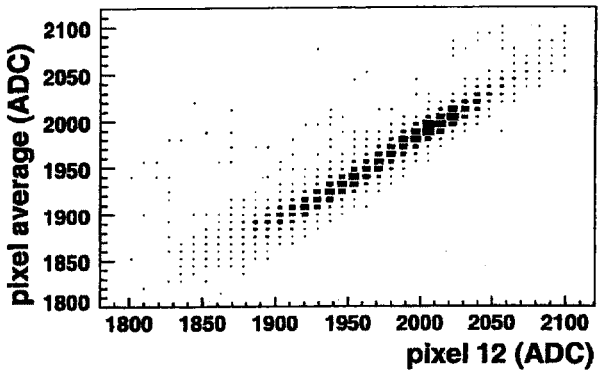


Fig. 7. Coherent noise in the system. Read out of a single pixel versus average of pixels of a double column.

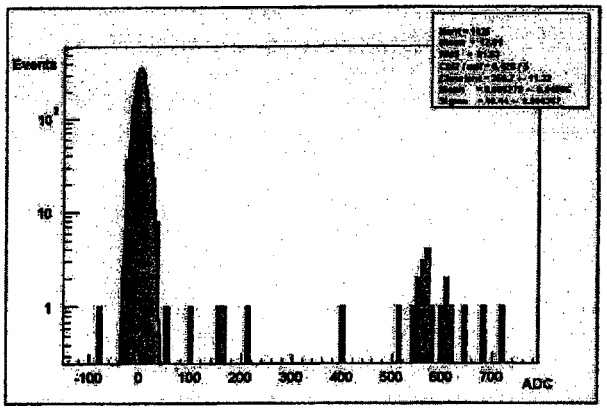


Fig. 8. Signal-to-noise ratio for a single pixel of roughly 55 was found after coherent noise corrections were applied.

Fig. 8 shows the output of a single pixel after pedestal subtraction. Two peaks are clearly visible. The one centered at 0 has a $\sigma$ of 10.5ADC that is a direct measurement of the noise. The other peaked at 600ADC, is the collected signal. This results in a signal to noise ratio of roughly 55. Taking the calibration results mentioned earlier this translate into a signal of about 10 $Ke^-$. This was not due to charge collection inefficiency, but to the analog part of the chip being saturated. This is supported by Fig. 9, where the total cluster charge is plotted versus the hit position along a column. The amount of charge collected when the track passed trough the p-stop regions is twice as much what is collected when the hit is in the center of a pixel. Such a behavior can only be explained by a

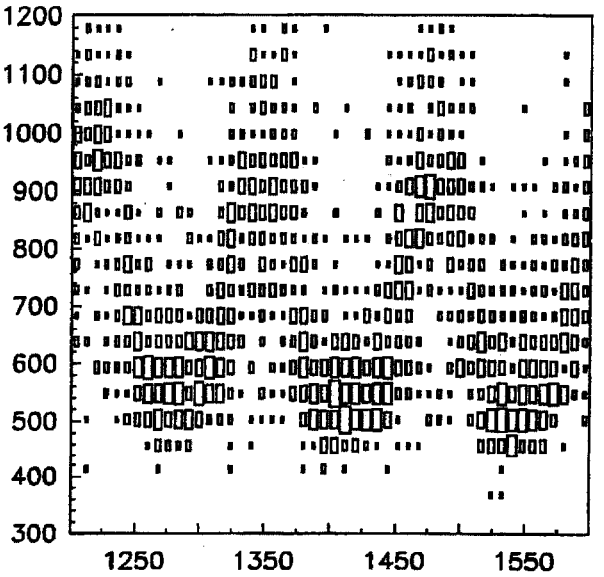


Fig. 9. This plot shows the total cluster charge in ADC collected versus the hit position along a column in microns. The total cluster charge is increased whenever charge is shared and indicates saturation.

saturated FE electronic. The level of saturation was a result of our selection of the parameter settings which were optimized on the signal-to-noise ratio.

### *4.4. Charge sharing and resolution*

In every event we looked for the pixel in a double column that returned the largest pulse height after pedestal correction $PH_c$. This pixel was called the center hit pixel. The pulse height of its left and right neighbor in the double column were denoted $PH_l$ and $PH_r$, respectively. Left was defined as the positive direction of the $x$-axis. The rotation was in such a way that the left (right) side was moved towards (away from) the incoming beam. Therefore, particles were entering the pixel sensors on the left side once the pixels were rotated, with respect to the beam direction. The fraction of charge deposited in the adjacent pixels $(PH_l/(PH_c + PH_l) + PH_r/(PH_c + PH_r))$ can be seen in Fig. 10, for the pixel array non-rotated ($\alpha = 0°$). In comparison the fraction of the charge deposited in the neighboring pixel for the rotated

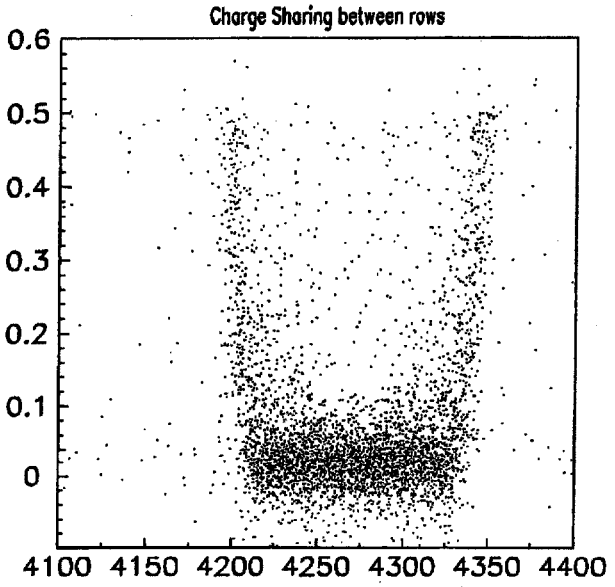


Fig. 10. Fraction of charge deposited in a neighboring pixel (row) versus the track position in micrometer. The scale has an arbitrary offset. The plot shows charge sharing for $\alpha = 0°$.

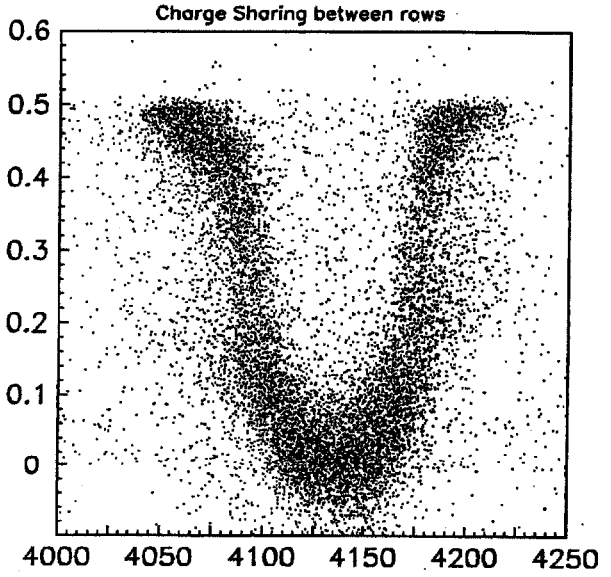


Fig. 11. Fraction of charge deposited in a neighboring pixel (row) versus the track position in micrometer. The scale has an arbitrary offset. The plot shows charge sharing for $\alpha = 20°$.

case ($\alpha = 20°$) is shown in Fig. 11. As expected charge sharing increased as the sensor was rotated.

*4.4.1. Observed charge sharing distribution*

The charge deposited in the center hit pixel and its neighbors could be used to locate the particle track with higher precision and therefore increased the resolution. There exist different ways to correct for the position using charge sharing. One of the simplest methods to correct the hit position is by finding the "center of mass" of the hit. A more accurate way is to use the charge distribution itself to determine the position, as done here. The charge division between three pixels in a column was described in terms of a parameter $\eta$ defined by

$$\eta = \frac{\mathrm{PH_l}}{\mathrm{PH_c} + \mathrm{PH_l}} - \frac{\mathrm{PH_r}}{\mathrm{PH_c} + \mathrm{PH_r}}. \quad (1)$$

The probability that a fraction of charge was shared between the pixels was found experimentally by plotting the number of events corresponding to a certain value of $\eta$. The resulting distribution $W(\eta)$ is shown in Fig. 12 for the non-rotated sensor and Fig. 13 for $\alpha = 20°$.

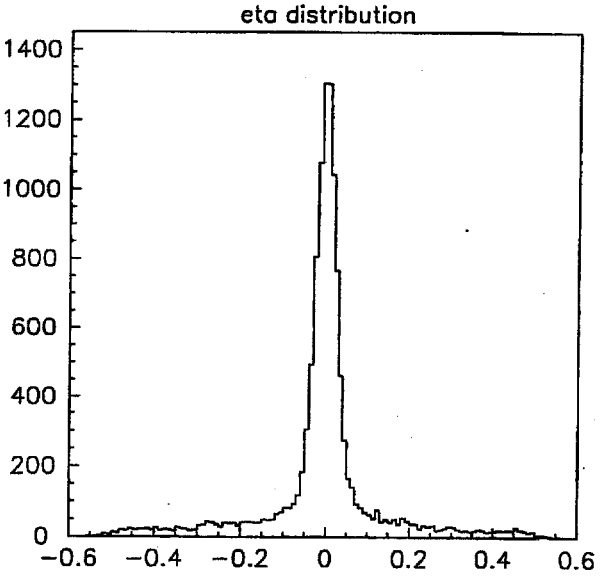


Fig. 12. $W(\eta)$ distribution for non-rotated detector.

It was found that there are very few hits that deposit charge in more then two pixels in one column (along $x$-axis) in an event. This was

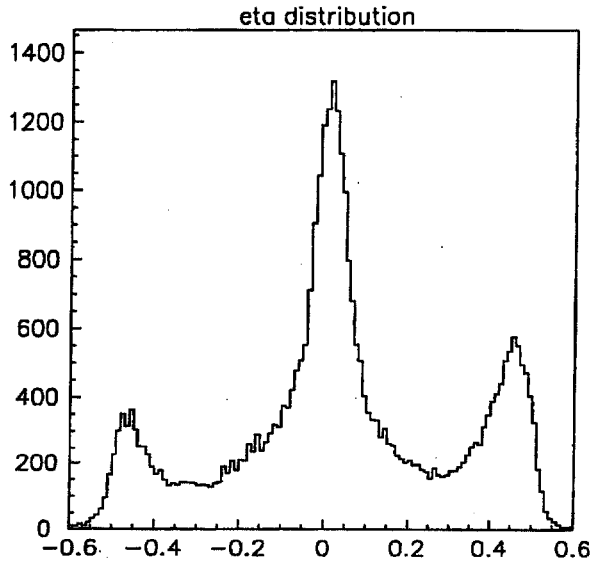


Fig. 13. $W(\eta)$ distribution for detector at 20°.

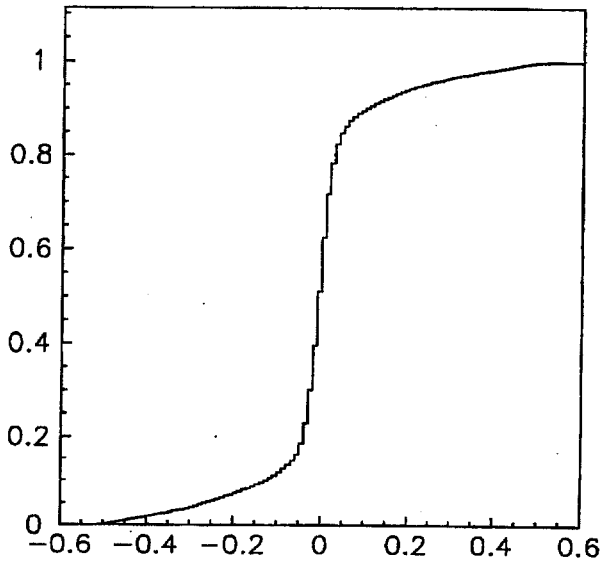


Fig. 14. $P(\eta)$ is the position correction function used to interpolate a pixel hit position using charge sharing between the neighboring pixels of a row . The plot shows $P(\eta)$ for $\alpha = 0°$.

expected by geometric considerations. Nevertheless the studies done here are using an $\eta$ that involves the pulse height of the center hit pixel and those of its left and right neighbor. $\eta$ was chosen in this way to be better able to compare directly differences in the adjacent pixels. Using a distribution of the charge collected by just two pixels would increase the resolution slightly, because it eliminates the third pixel that contributes only noise. Besides the peak at $\eta = 0$ we observe two lateral peaks at $\eta \simeq \pm 0.45$, an explanation for those peaks is given in Section 4.4.2.

The resulting distribution $W(\eta)$ was used to increase the resolution of the pixels by making use of the assumption that it is equally likely that a hit occurs anywhere in the pixel. Since the pixels were small compared to the beam size we can assume that the hit distribution within a pixel was homogeneous. By integrating over the distribution $W(\eta)$ one gets a position correction function $P(\eta)$ defined by

$$P(\eta) = \frac{1}{A} \int_{-\infty}^{\eta} \mathrm{d}y \, W(y). \tag{2}$$

Figs. 14 and 15 show the position correction function $P(\eta)$, which was normalized to one using the normalization constant $A = \int_{-\infty}^{\infty} \mathrm{d}y \, W(y)$. By

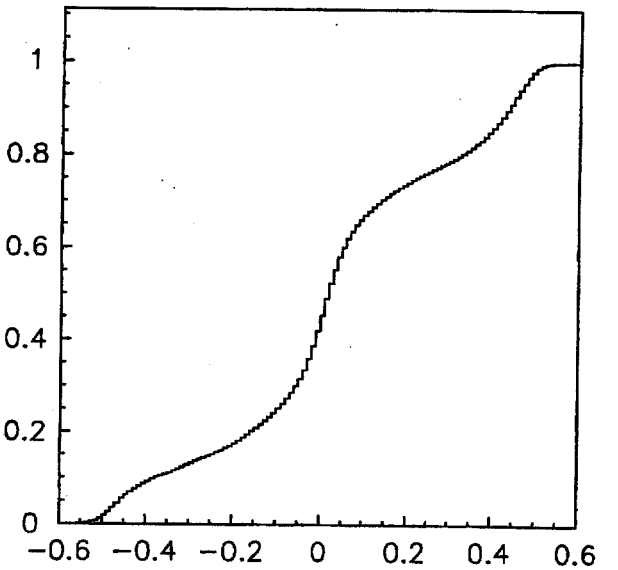


Fig. 15. $P(\eta)$ is the position correction function used to interpolate a pixel hit position using charge sharing between the neighboring pixels of a row . The plot shows $P(\eta)$ for $\alpha = 20°$.

calculating $\eta$ in an event the corrected hit position was found with the following equation:

$$x'_{\text{corrected}} = x' + P(\eta) x_{\text{pitch}}, \tag{3}$$

where $x'$ is the position between the right and center pixel and $x_{\text{pitch}}$ is the pixel pitch, which is 150 μm. In the following analysis the resolution was measured in the sensor coordinate system. Therefore, the position obtained by the tracking telescope was multiplied by $1/\cos(20°)$ to project it into the sensor coordinate system. To obtain the resolution in the telescope system, which also corresponds to the resolution in $r$–$\phi$ then we have to multiply the given values by a factor of $\cos(20°) \simeq 0.94$.

*4.4.2. Description of the charge sharing distribution*

A parametric simulation has been performed to reproduce the observed $W(\eta)$ distribution. The parametric simulation has been conducted to understand the following questions related to the observed distribution of $W(\eta)$ for the sensor at $\alpha = 20°$ (Fig. 13):

- Why do we observe two lateral peaks?
- Why do they peak at $\pm 0.45$?
- Why do the lateral peaks are asymmetric?

The parametric simulation was able to reproduce the observed distribution with experimentally motivated input parameters. The charge collected in a pixel was calculated from a Landau distribution with a linear shift of the center according to the track length in the pixel.

Under the assumption of a perfect detector (no noise and no saturation) the $W(\eta)$ distribution shown in Fig. 16 (dash dotted line) is produced. The central peak is created by events that only deposit charge in one pixel. The rest of the distribution with $\eta$ different from zero are caused by events that share charge. When adding the saturation to the simulation, the two lateral peaks appear at $\eta = \pm 0.5$. They are created when two pixels are saturating, the central hit pixel and an adjacent pixel, this distribution is shown in Fig. 16 (solid line). If noise is introduced, it leads to a broadening of the peaks and also introduces a shift of the peaks as seen in Fig. 16 (dashed line). This is mostly due to dependence of the distribution $W(\eta)$ on the definition of the center hit pixel. If two pixel saturate but return a different signal due to noise then $|\eta|$ will be lowered because the center hit pixel

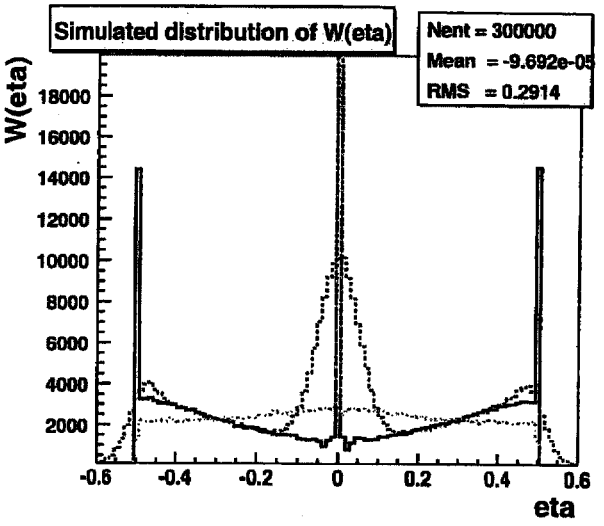


Fig. 16. Results of the parametric simulation with no noise and no saturation (dash-dotted), saturation and no noise (solid) and saturation and noise (dashed).

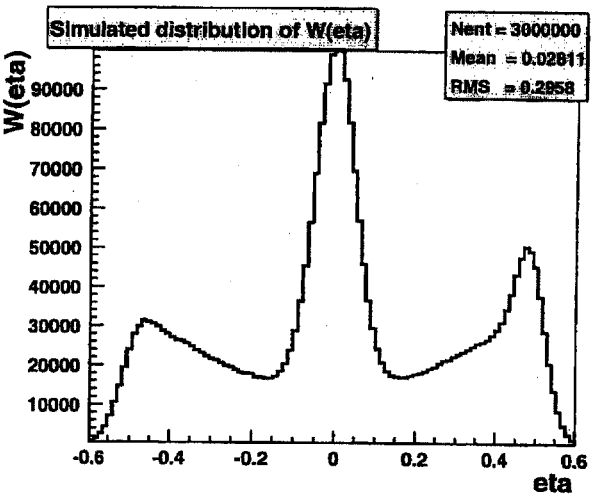


Fig. 17. Simulation results using saturation, noise, common mode noise, saturation (at different levels for adjacent pixels) with experimentally motivated values.

will always be chosen as the one with the highest signal. An asymmetry in the lateral peaks can be introduced by using different saturation levels for the pixels. If we assume there is a 2% difference in the saturation between two adjacent pixels then we get the distribution shown in Fig. 17. This effect

can be associated with an observed sagging of the pedestal, that was in the order of one to two percent difference in the pedestal levels of two adjacent pixels. This effect is under further investigation.

### *4.5. Results*

The resolution was calculated by comparing the track position interpolated by the silicon strips and the pixel hit position calculated using charge sharing between rows. The difference was fitted to a Gaussian. The resolution of the telescope has a negligible effect on this resolution measurement. The pixel resolution using the position correction curve is shown in Fig. 18 for $\alpha = 0°$ and for $\alpha = 20°$ in Fig. 19. It can be seen that we obtain a resolution of $\sigma = 17$ μm for the sensor rotated by 20°. This value is in agreement with simulations [6], that find a $r$–$\phi$ resolution of 18 μm for pixel in the blade. Fig. 20 shows the resolution as a function of the hit position and Fig. 21 as a function of the fraction of charge shared. It can be seen that for $\alpha = 20°$ the resolution is between 10 and 20 μm. There is no large variation in the

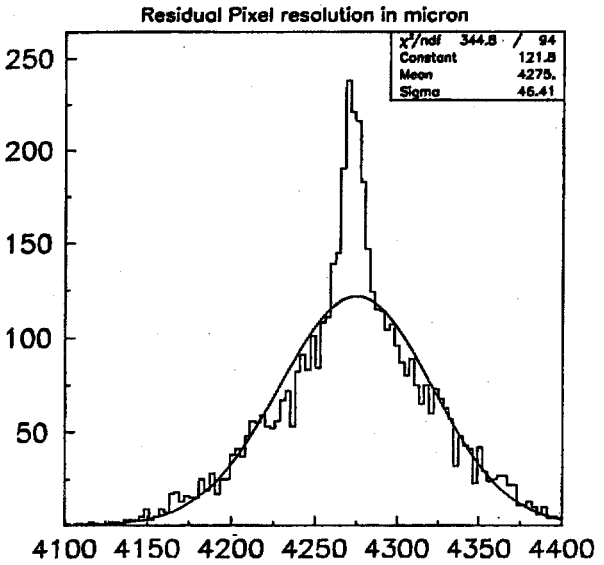


Fig. 18. A resolution of 46 μm is found along columns for $\alpha = 0°$ using charge sharing. The peak at the center indicates a higher resolution in case charge was shared with neighboring pixels.

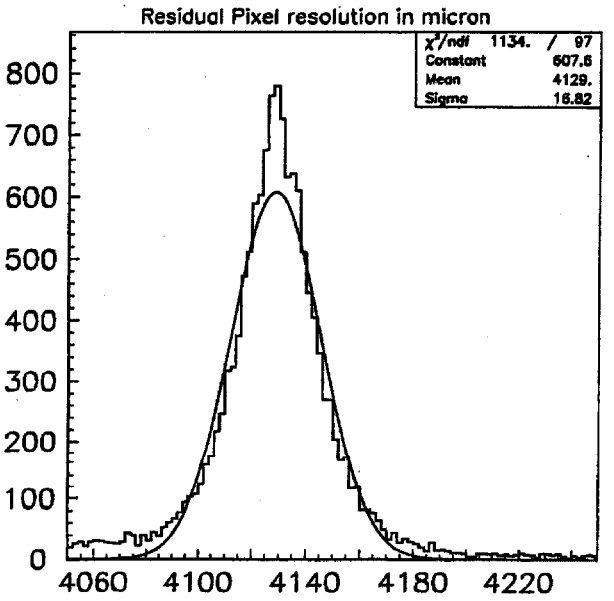


Fig. 19. An average resolution of 17 μm is found along columns for $\alpha = 20°$ using charge sharing.

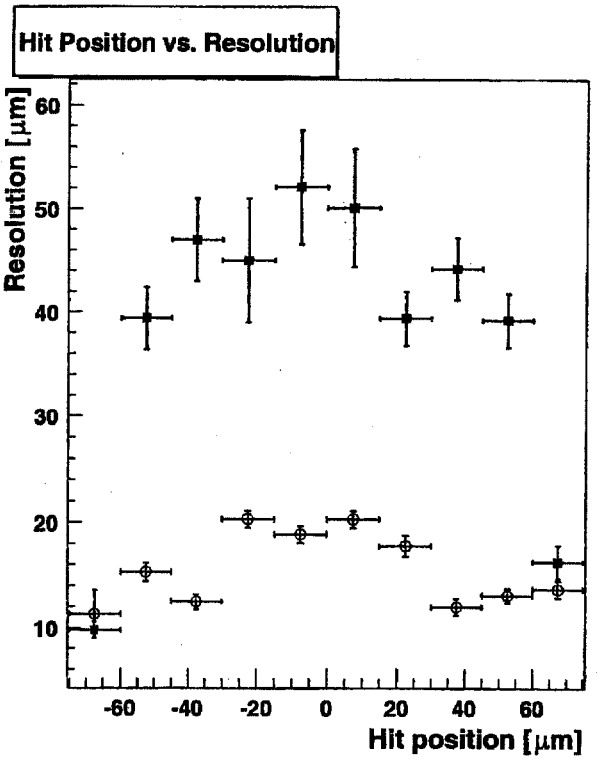


Fig. 20. Comparison of resolution vs. hit position for beam at 0° (box) and 20° (circle) incidence.

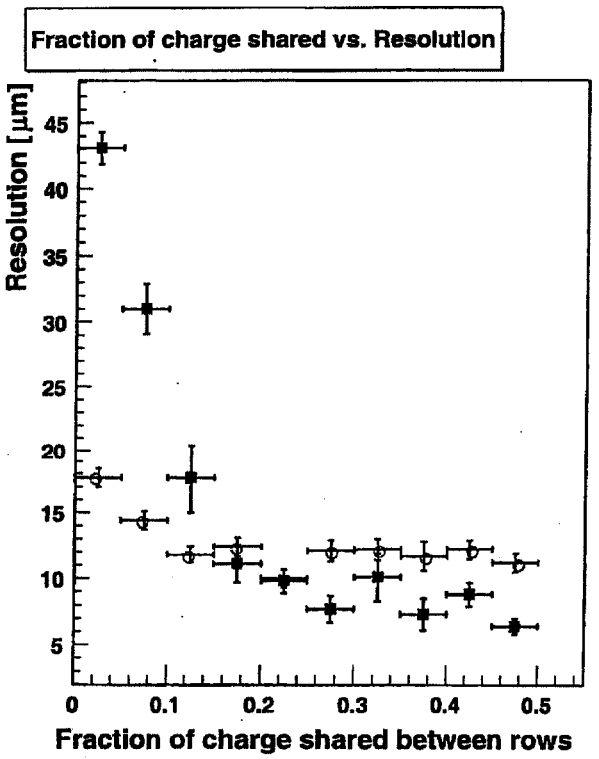


Fig. 21. Comparison of resolution vs. fraction of charge shared for beam at 0° (box) and 20° (circle) incidence.

resolution over the amount of charge shared. This can be understood by looking at the slope of the position correction curve seen in Fig. 15, which shows a more constant slope compared to $\alpha = 0°$. In case of $\alpha = 0°$ seen in Fig. 14 only a small region shares charge, therefore the difference in the slope in the position correction curve is larger which results in a more dramatic change of the resolution versus the amount of charge shared. Hence, for the non-rotated case a resolution between 10 and 50 μm was found. It has to be noted that for the non-rotated case most of the events have very little charge sharing but for those events that fall into the region between two pixels the resolution is greatly improved (as seen from Figs. 20 and 21). These plots indicate that a resolution of about 10 μm is achievable. By examining the resolution versus the position of the hit one can see that the center region of the pixel (0 is the center of the hit pixel) has the lowest resolution. A resolution between 40 and 50 μm is found in the center region of the non-rotated detector. This is in agreement with the theoretical expected resolution for pixel without charge sharing, at $150\ \mu m/\sqrt{12} \simeq 43\ \mu m$. The resolution shown here is the resolution along columns as a result of charge sharing between rows. The resolution along a row could not be studied extensively, since most of the data were taken with only one double column enabled. Nevertheless, we do not expect any differences in the resolution along rows.

## 5. Conclusions

Non-irradiated silicon pixels bump bonded to DMILL readout chips for the CMS forward pixel detector have been tested in a beam at CERN. A tracking telescope was used to interpolate particle tracks. The DMILL readout chip (PSI 36) was found to be noisy and it was challenging to read out multiple double columns, since this further increased the noise in the system. Coherent noise in the system was observed. After correction for coherent noise, a $S/N$ of $\sim 55$ was found. Using charge sharing a resolution of 10–50 μm was achieved along rows for the non-rotated case, depending on the hit position. Similarly, for the sensor rotated at a 20° angle resolutions of 10–20 μm were found. The charge sharing distribution could be reproduced using a parametric simulation. The results remain to be verified with irradiated detectors. Detectors for the forward pixel detector have been irradiated and will be tested in a future beam test. Also the effect of the magnetic field has yet to be fully investigated.

For future beam tests it will also be important to have the ability to rotate the sensor around the vertical axis as well as the horizontal axis. Charge sharing can then be investigated for a situation similar to the final setup in the CMS forward disks.

In the final setup there will be geometric charge sharing in both the pixel row and column coordinates. This is due to the 20° blade rotation as well as the geometric offset of the detectors with respect to the primary vertex.

## References


[1] CMS Collaboration, CMS-The Tracker Project-Technical Design Report, CERN/LHC98-6.

[2] D. Bortoletto, et al., Nucl. Instr. and Meth. A 461 (2001) 182.

[3] R. Horisberger, Nucl. Instr. and Meth. A 465 (2001) 148.

[4] RD42 Collaboration, W. Adam et al., Nucl. Instr. and Meth. A 465 (2001) 88.

[5] W. Karpinski et al., Performance studies of pixel readout electronics in RICMOS IV-SOI and DMILL processes, 5th Workshop on Electronics for the LHC Experiments (LEB 99), Snowmass, CO, USA, 20–24 September 1999; in: Snowmass 1999, Electronics for LHC Experiments, pp 103–107; CERN 99-09, CERN/LHCC/99-33, 29 Oct. 1999.

[6] Report of the US CMS Forward Pixel Detector for the US CMS DOE/NSF Review FNAL, May 19–21, 1997.